Supplementary Information (SI) for Journal of Materials Chemistry B.

Supporting information

Near-infrared fluorescent-photoacoustic nanoprobe for tumor targeted photodynamic-photothermal therapy

Di Zhao,[a] Yingzhong Zhu,[a,b] Shunyi Wang,[a] Qiuqi Gao,[c] Wanyang Li,[c] Han Yang,[d] Bo Wu,[c]* Lin Kong,[a]* Changjie Mao[a]*

[a] School of Chemistry and Chemical Engineering, Anhui University, Hefei, Anhui 230039, PR China.

[b] School of Materials and Chemical Engineering, ChuZhou University, Chu Zhou Anhui 239000, China.

[c] School of Environmental and Chemical Engineering, Wuyi University, Jiangmen 529020, PR China.

[d] Department of Chemistry, Department of Chemical and Biological Engineering, Hong Kong Branch of Chinese National Engineering Research Center for Tissue Restoration and Reconstruction, and State Key Laboratory of Nervous System Disorders, The Hong Kong University of Science and Technology, ClearWater Bay, Kowloon, Hong Kong 999077, China.

Correspondence and requests for materials should be addressed to L.K. (email: wubo@wyu.edu.cn, konglin@ahu.edu.cn)

Content

S1. Material Synthesis

S2. Optical Properties

S3. Photothermal Conversion and Photoacoustic Signals

S4. Theoretical Calculations

S5. Cytotoxicity Assays

S6. In Vivo Imaging

S7. In Vivo Phototherapy

S1. Material Synthesis

Synthesis of intermediate CyCl: Phosphorus oxychloride ($POCl_3$, 15 mL, 162 mmol) was added dropwise under an ice bath cooling to a stirred solution of N,N-dimethylformamide (DMF, 16 mL) and dichloromethane (DCM, 16 mL) in a 100 mL round-bottom flask, utilizing a constant-pressure dropping funnel [S1]. Following the complete addition of $POCl_3$, cyclohexanone (4.00 g, 40 mmol) was introduced to the mixture. The reaction mixture was maintained in the ice bath for an additional 5 minutes, then heated to reflux and stirred for 3 hours. The reaction progress was monitored by thin-layer chromatography (TLC). Upon completion, the reaction mixture was poured into an ice-water bath and stirred overnight, affording a bright yellow precipitate, which was collected by vacuum filtration, and dried under reduced pressure. The resulting crude product was stored at -20 °C and employed directly in the subsequent synthetic step without further purification.

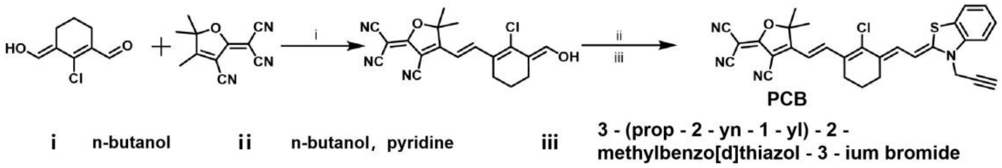

Fig. S1. Synthetic route of the PCB.

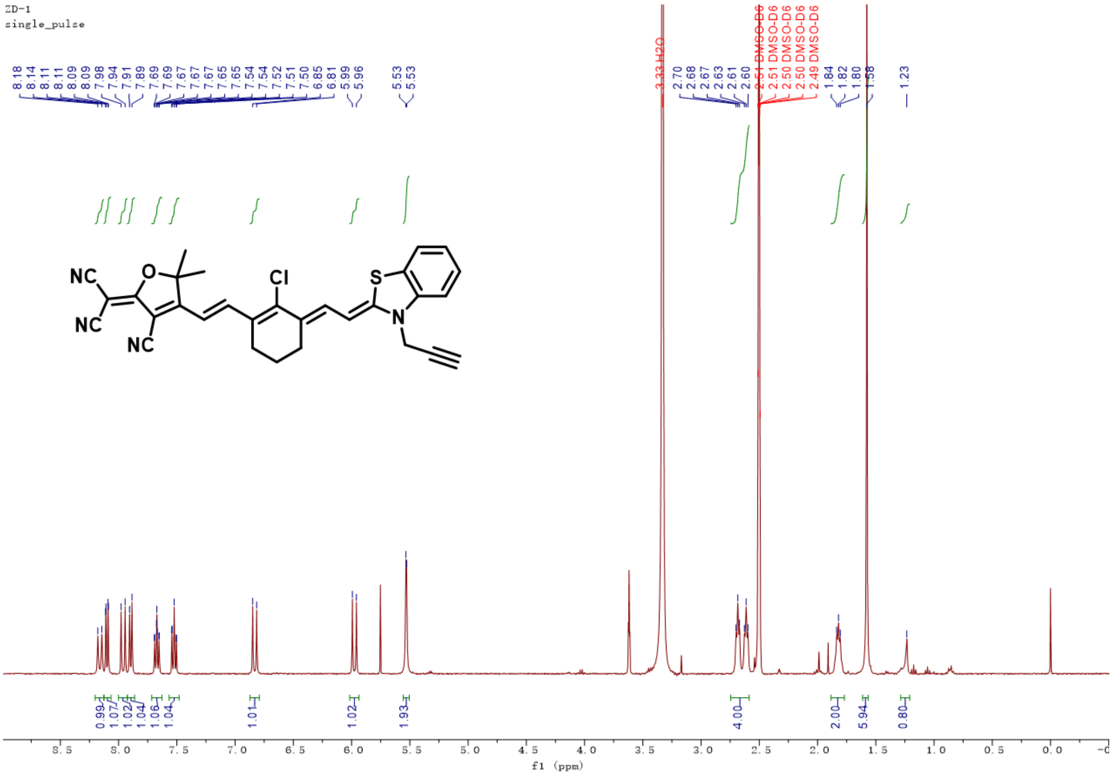

Fig. S2. ^{1}H NMR spectrum of PCB in d_6-DMSO (600 MHz).

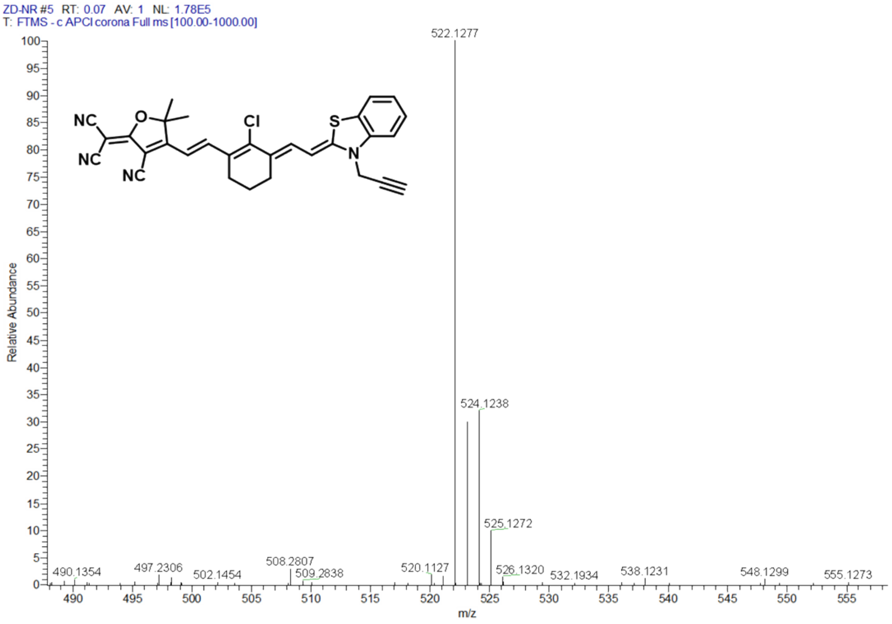

Fig. S3. Mass Spectrum of PCB.

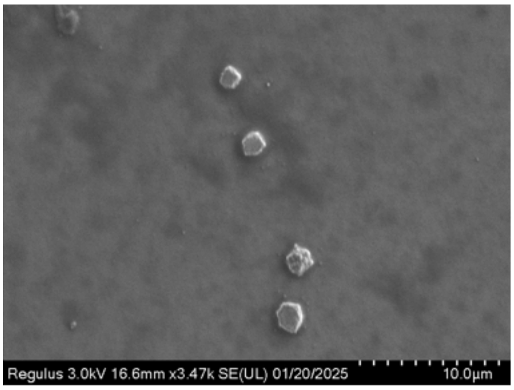

Fig. S4. SEM image of DSPE-PEG-cRGD.

S2. Optical Properties

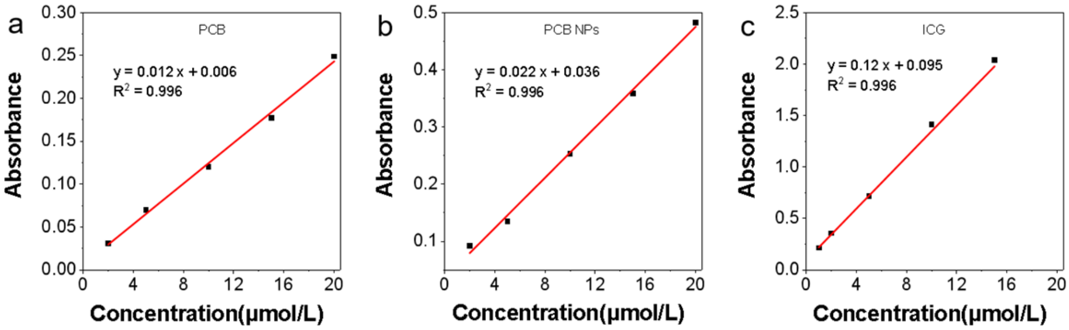

Fig. S5. Concentration-absorbance working curves of (a) PCB, (b) PCB NPs, (c) ICG.

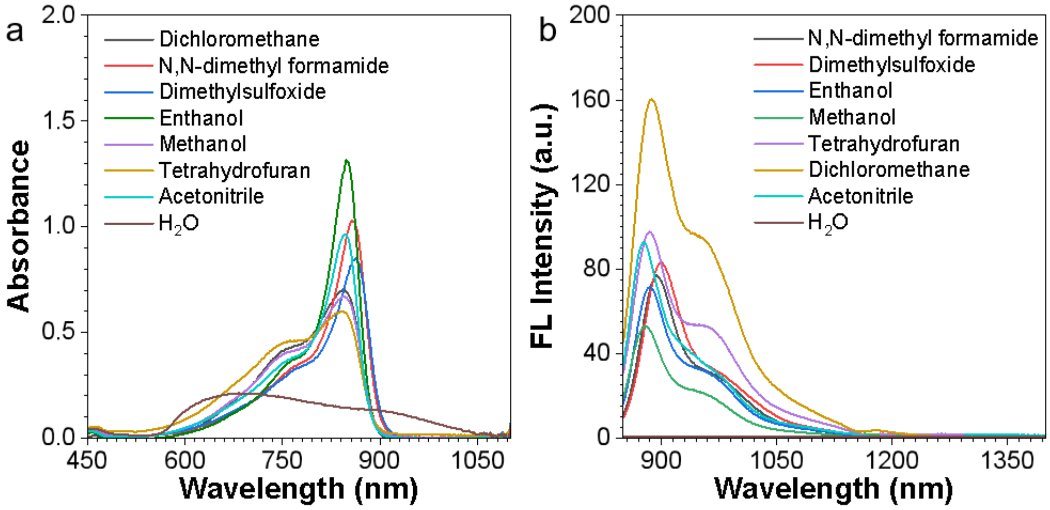

Fig. S6. (a) The absorption spectra of PCB in different solvents. (b) Emission spectra of PCB in different solvents. c = 1.0×10^{-5} mol·L^{-1}

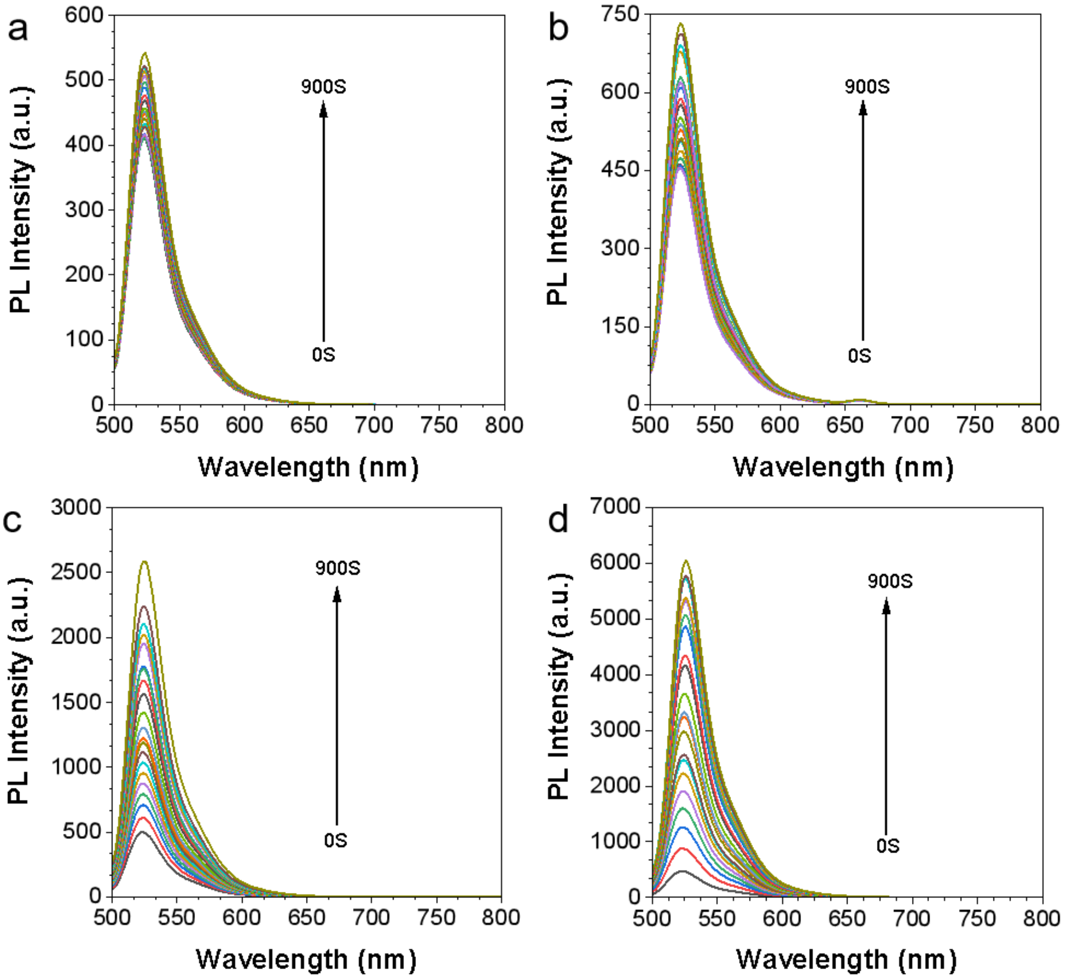

Fig. S7. Fluorescence emission spectra of (a) DCFDA, (b) Ce6+DCFDA, (c) PCB+DCFDA, and (d) PCB NPs+DCFDA in DMSO/PBS mixed solvent under laser irradiation and aerobic conditions. λ_{ex}: 808 nm (0.8 W cm^{-2}).

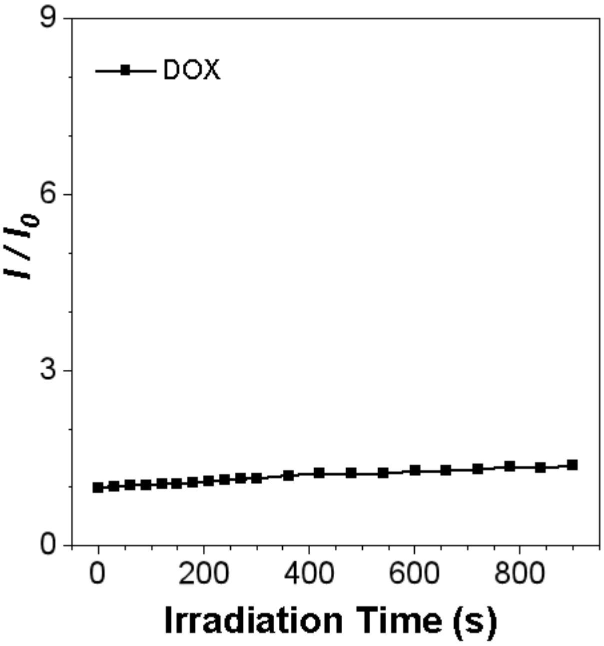

Fig. S8. Time-dependent fluorescence intensity (I / I₀) of DCFDA-DOX under normoxia. λ_{ex}: 808 nm (0.8 W cm^{-2}).

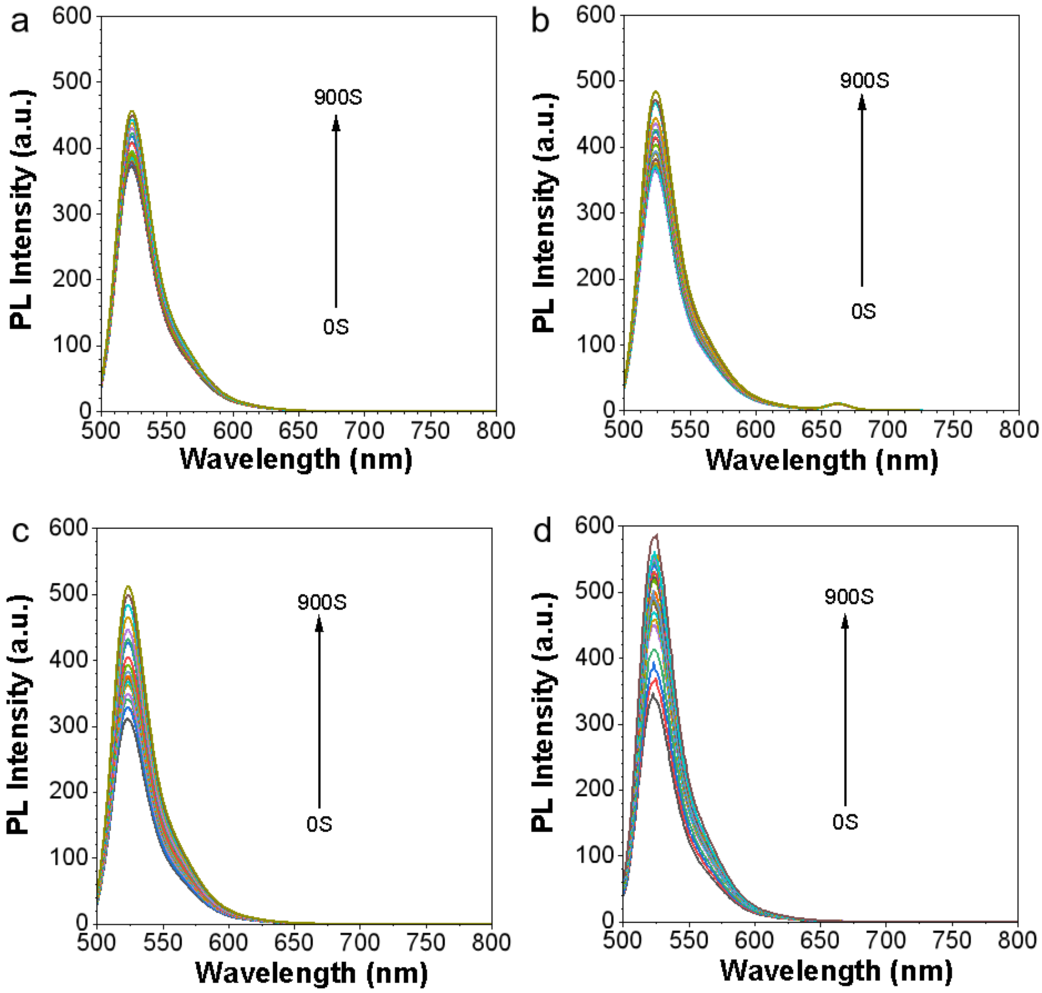

Fig. S9. Fluorescence emission spectra of (a) DCFDA, (b) Ce6+DCFDA, (c) PCB+DCFDA, and (d) PCB NPs+DCFDA in DMSO/PBS mixed solvent under laser irradiation and hypoxic conditions. λ_{ex}: 808 nm (0.8 W cm^{-2}).

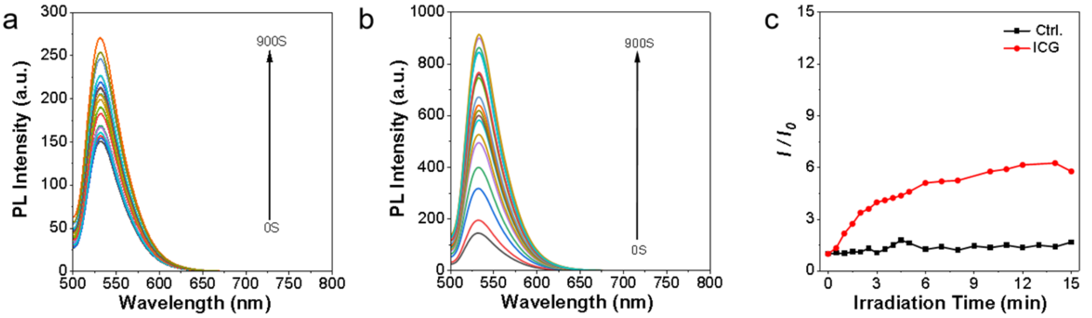

Fig. S10. Fluorescence emission spectra of (a) DCF-DA, (b) ICG+DCF-DA in DMSO/PBS mixed solvent under laser irradiation. (c) Time-dependent fluorescence intensity (I/I_0) vs irradiation time of (a) and (b). λ_{ex}: 808 nm (0.8 W cm^{-2}).

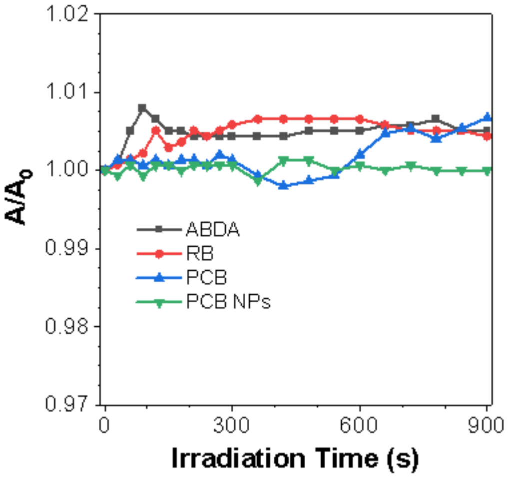

Fig. S11. The degradation curve of 4-Azido-2,3,5,6-tetrafluorobenzoic acid (ABDA) under different light irradiation durations, λ_{ex}: 808 nm (0.8 W cm^{-2}).

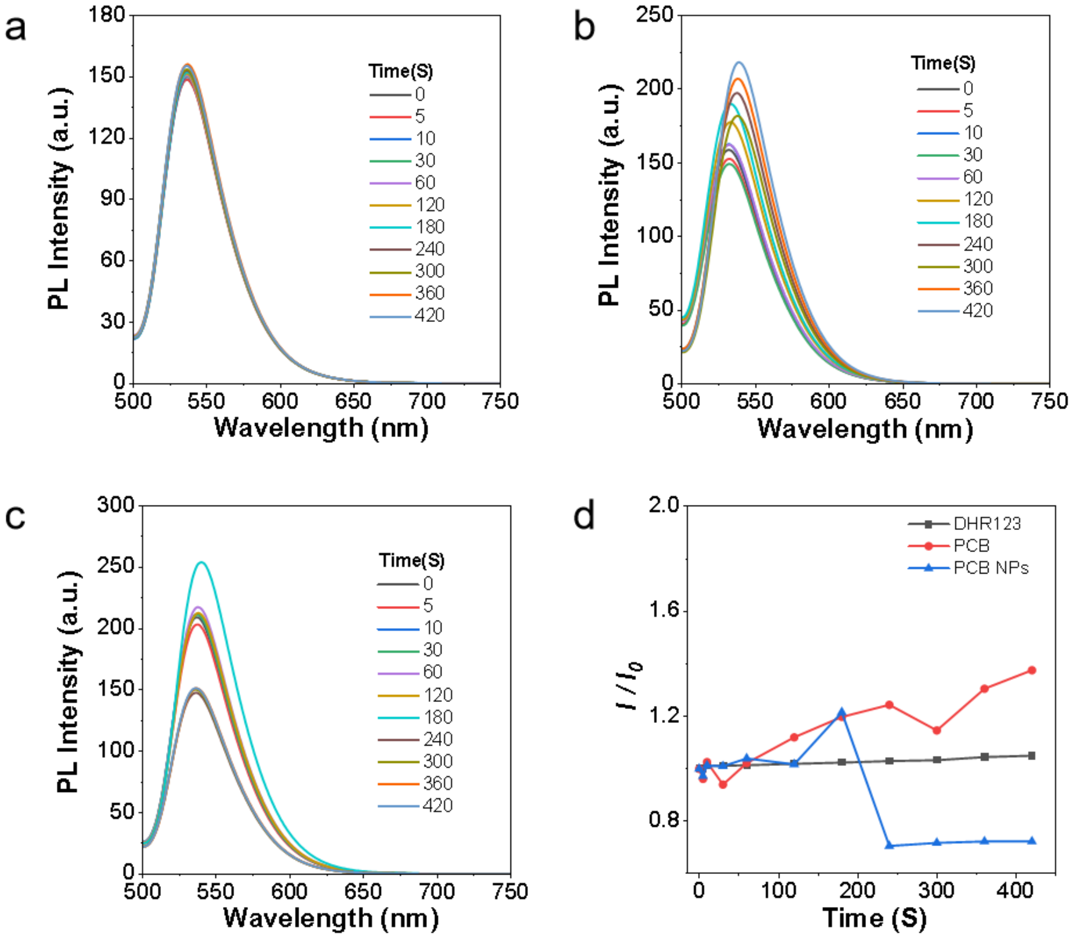

Fig. S12. (a) Fluorescence spectra of aqueous solutions containing only DHR 123 under different illumination times. (b) Fluorescence spectra of aqueous solutions containing DHR 123 with a concentration of 10 μM PCB under different illumination times. (c) Fluorescence spectra of aqueous solutions containing DHR 123 with a concentration of 10 μM PCB NPs under different illumination times. (d) $O_2^{\bullet-}$ generation capacities of PCB and PCB NPs using DHR 123 as indicators, respectively.λ_{ex}: 808 nm (0.8 W cm^{-2}).

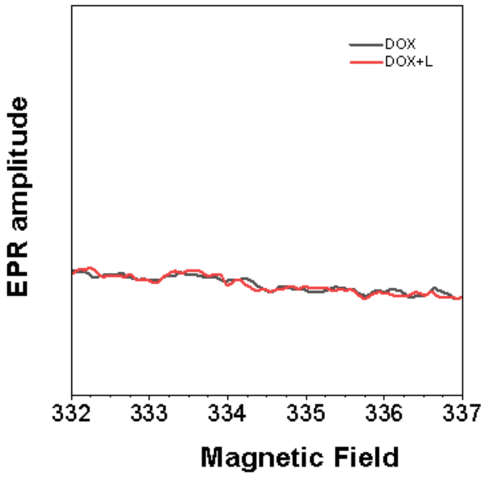

Fig. S13. Electron paramagnetic resonance (EPR) measurements of $O_2{\bullet}^-$ generation for DOX in the dark or after 5 min irradiation (808 nm, 0.8 W cm^{-2}) with 5,5-Dimethyl-1-pyrrolineN-oxide (DMPO) as the spin trapping agent.

S3. Photothermal Conversion and Photoacoustic Signals

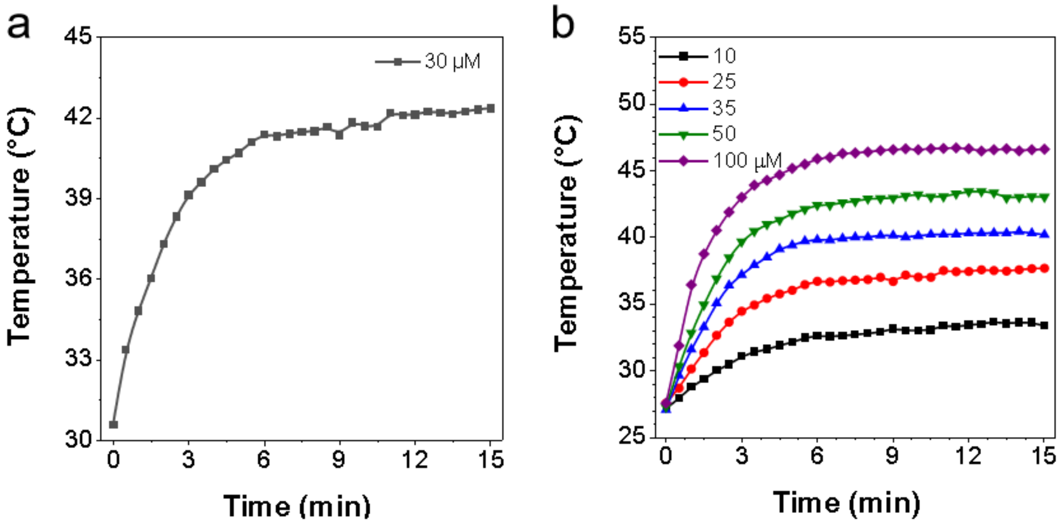

Fig. S14. Photothermal conversion. (a) Under 808 nm laser irradiation, the temperature change curves of the 30 μM PCB NPs in DMSO/H_2O (20% DMSO). (b) Temperature change curves of PCB NPs in DMSO/H_2O (20% DMSO) with different concentrations under 808 nm laser irradiation.

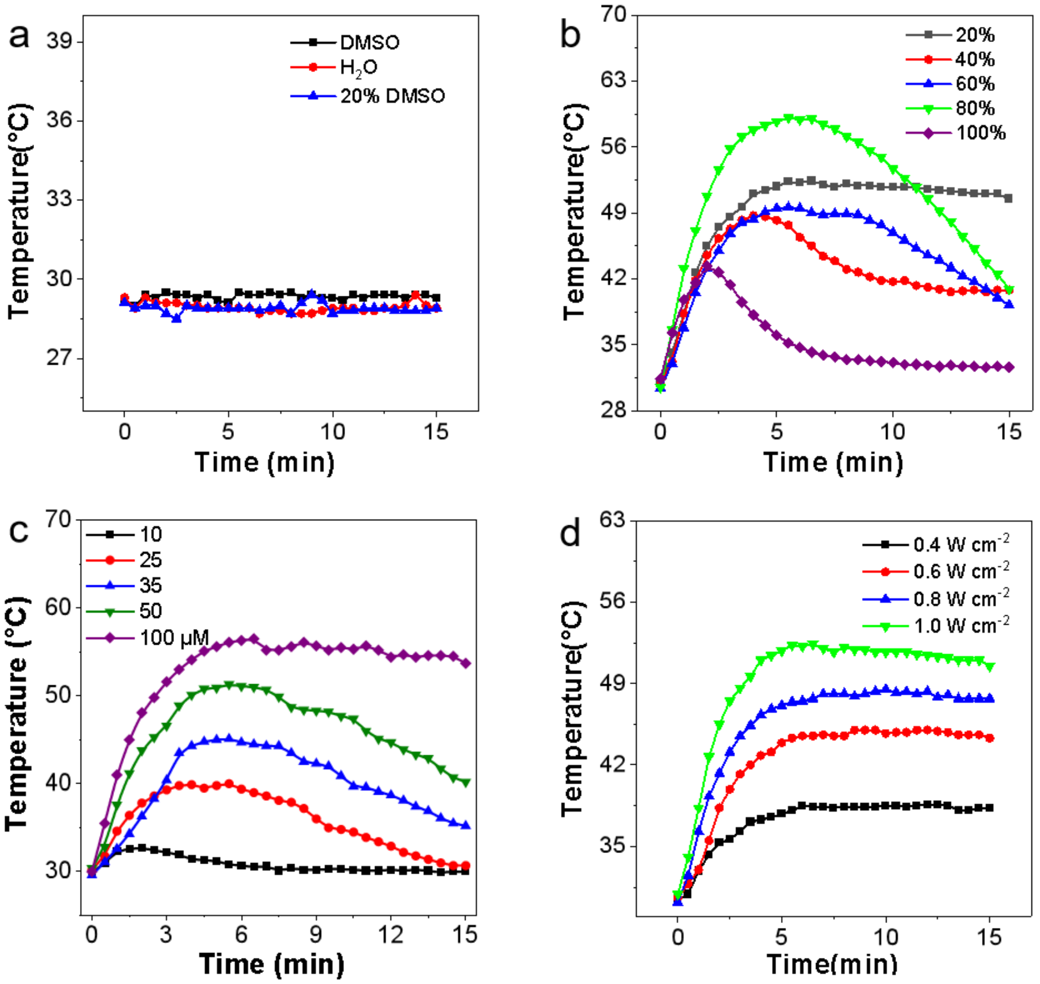

Fig. S15. Photothermal conversion. (a) Temperature change curves of PCB nanoparticle solutions in DMSO, H_2O, and 20% DMSO. (b) Temperature change curves of PCB with different DMSO/H_2O solvent ratios. (c) Temperature change curves of PCB in DMSO/H_2O (80% DMSO) with different concentrations. (d) Temperature change curves of PCB in DMSO/H_2O (20% DMSO) (100 μM) under 808 nm laser irradiation with different power densities. 0.8 W cm^{-2}, 15 min for (a) - (d).

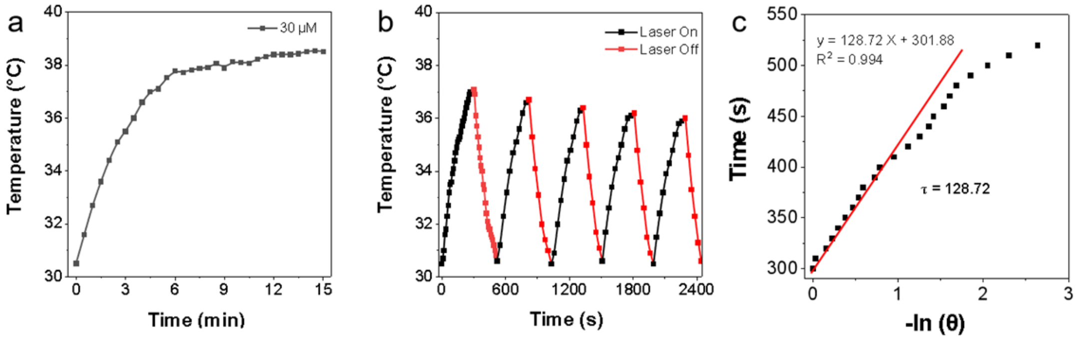

Fig. S16. Photothermal conversion. (a) The temperature of 30 μM PCB in DMSO/H_2O (20% DMSO). (b) Five successive photothermal heating/cooling cycles of PCB in DMSO/H_2O (20% DMSO). (c) Linear relationship between cooling time and -ln(θ) for PCB. 0.8 W cm^{-2}, 15 minutes.

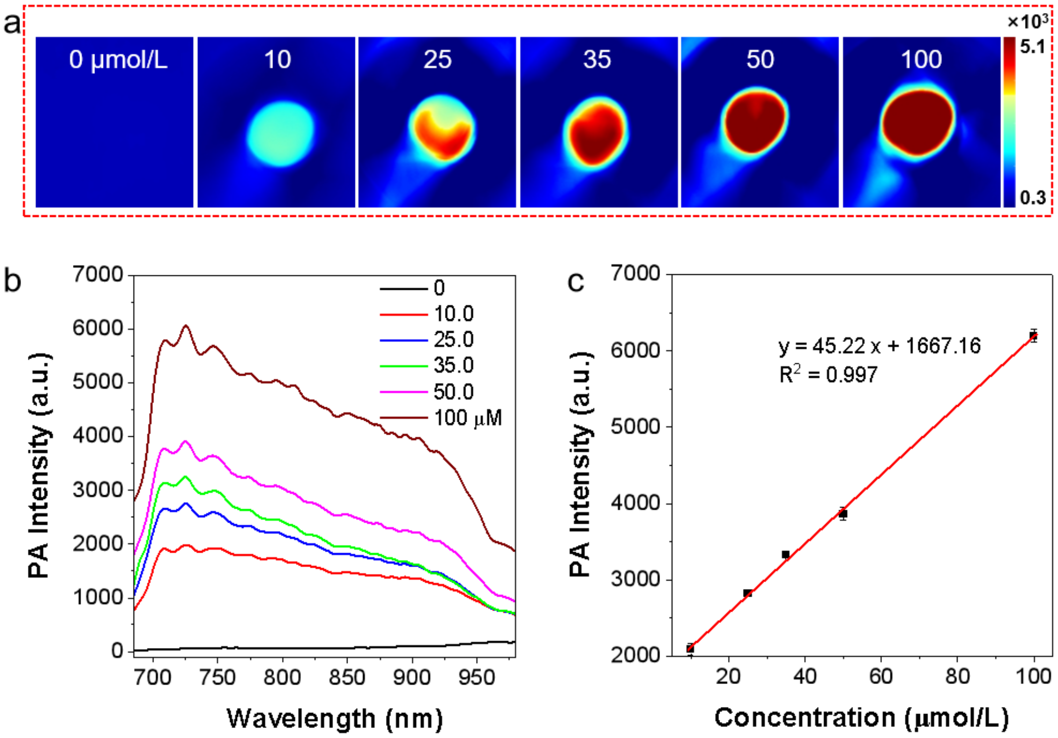

Fig. S17. (a) Photoacoustic (PA) images of PCB at different concentrations (0, 10, 25, 35, 50, 100 μmol/L). (b) PA signal curves (as a function of wavelength) of PCB at different concentrations. (c) Linear relationship plot between PA signal intensity and PCB concentration.

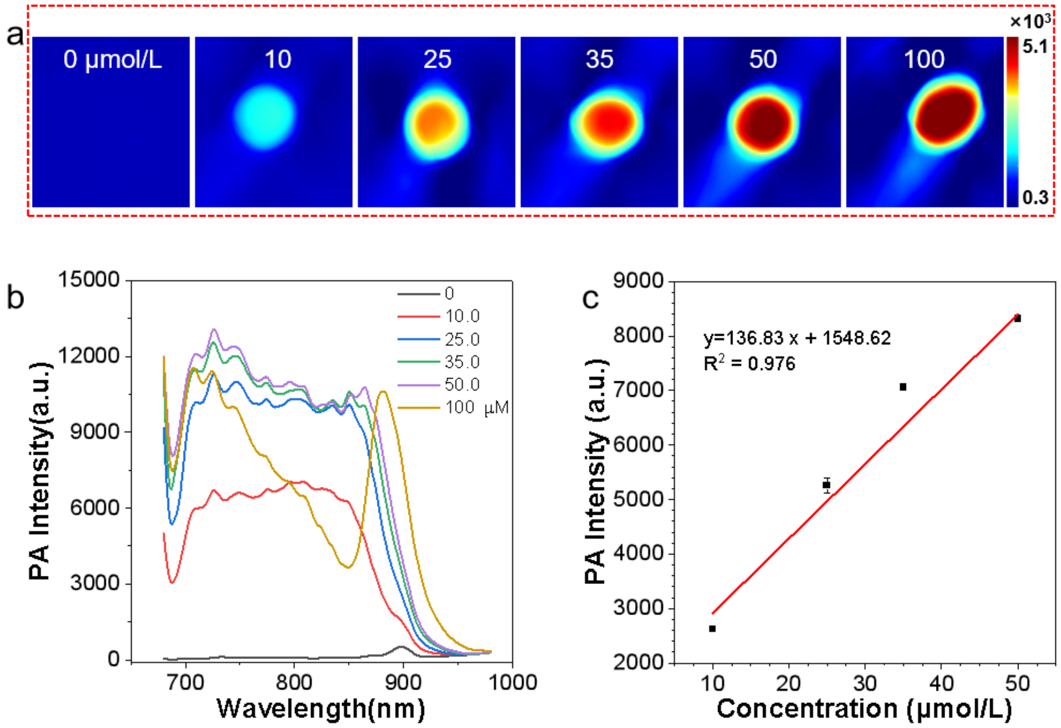

Fig. S18. (a) Photoacoustic (PA) images of PCB NPs at different concentrations (0, 10, 25, 35, 50, 100 μmol/L). (b) PA signal curves (as a function of wavelength) of PCB NPs at different concentrations. (c) Linear relationship plot between PA signal intensity and PCB NPs concentration.

S4. Theoretical Calculations

Table 19. Ground-State and Excited-State Energies and Related Parameters of ICG and PCB Systems (Unit: kcal/mol).

			Reorganization energy	**Energy from S_1 to CI**	**S_1 energy gap**
	E(S_0)	E(S_1)	lambda1+lambda2	δECI	
icg-s0-opt	0.00	47.17			
icg-s1-opt	4.51	44.74	6.95	22.70	40.23
icg-s1-ci	67.44	72.98			
pcb-s0-opt	0.00	48.22			
pcb-s1-opt	13.77	34.56	27.43	18.83	20.79
pcb-s1-ci	53.39	64.80			

S5. Cytotoxicity Assays

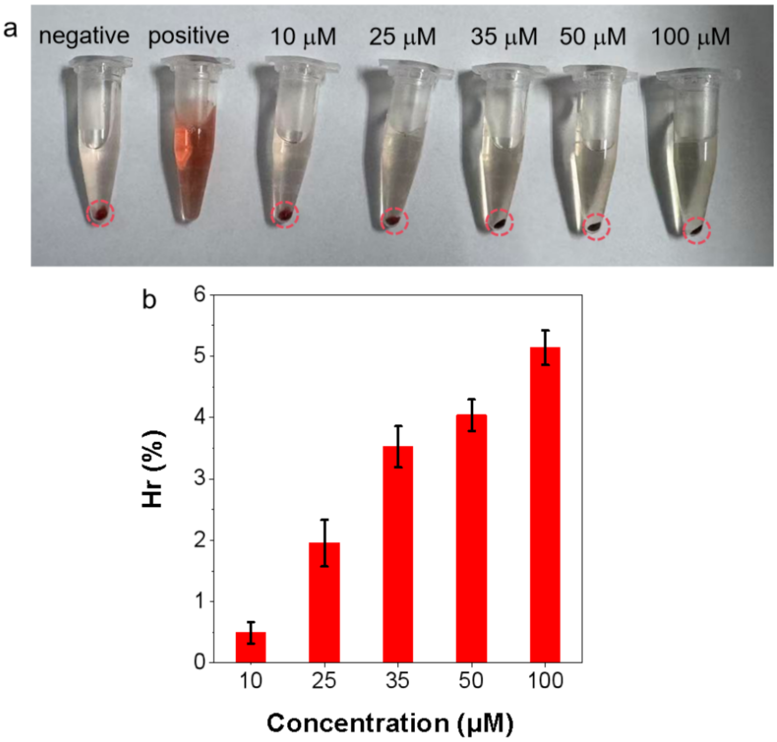

Fig. S20. (a) Hemolysis ratio of red blood cells incubated with PCB NPs (10, 25, 35, 50 and 100 μM). The negative control is PBS, and the positive control is water. (b) Image of red blood cells centrifugation and treatment with different concentrations of PCB NPs.

S6. In Vivo Imaging

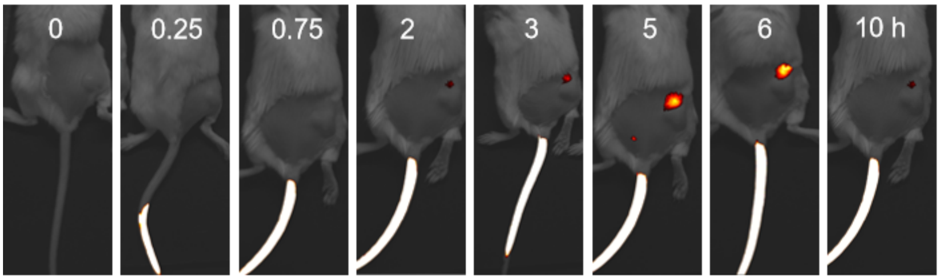

Fig. S21. Fluorescent images in mice following tail vein injection of PCB.

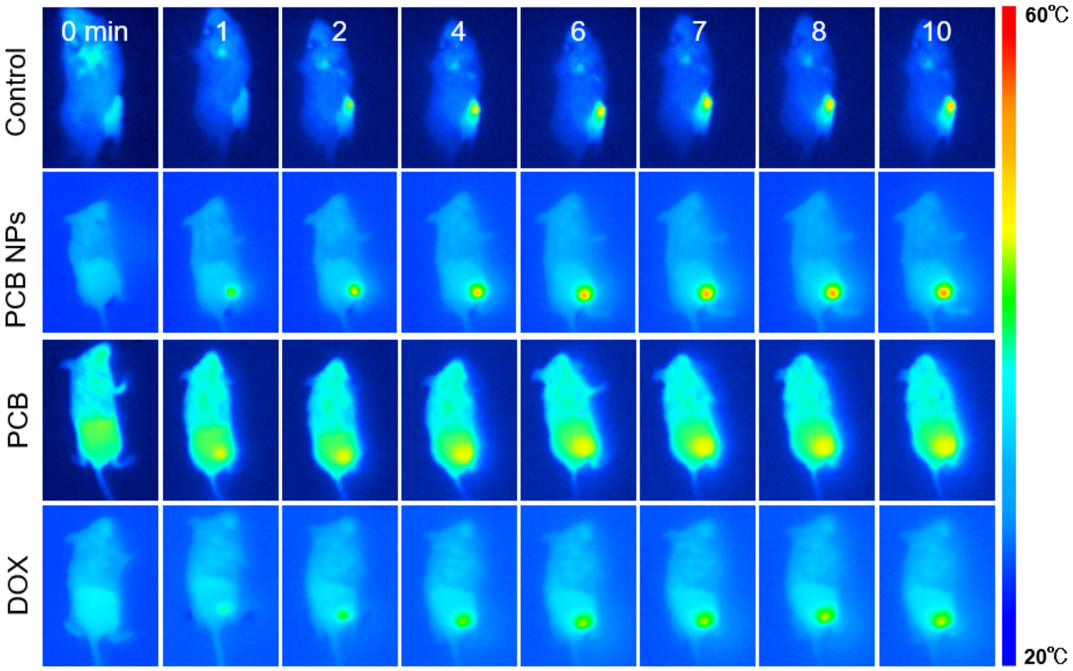

Fig. S22. Infrared thermal imaging images of tumor sites in 4T1 tumor-bearing mice after tail vein injection of PCB NPs, PCB, and DOX, followed by 808 nm laser irradiation (0.8 W cm^{-2}) for 10 minutes.

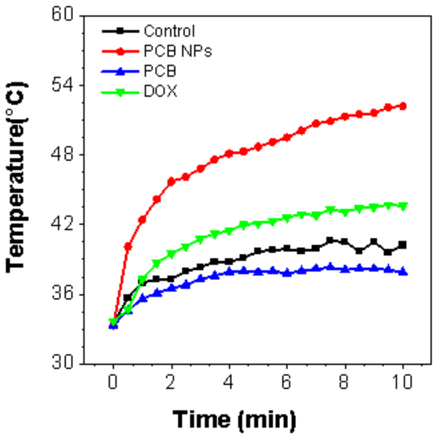

Fig. S23. Temperature change curves of the tumor region in 4T1 tumor-bearing mice without injection or after intravenous injection of PCB NPs, PCB, and Dox, upon 808 nm laser irradiation (0.8 W cm^{-2}) for 10 minutes.

S7. In Vivo Phototherapy

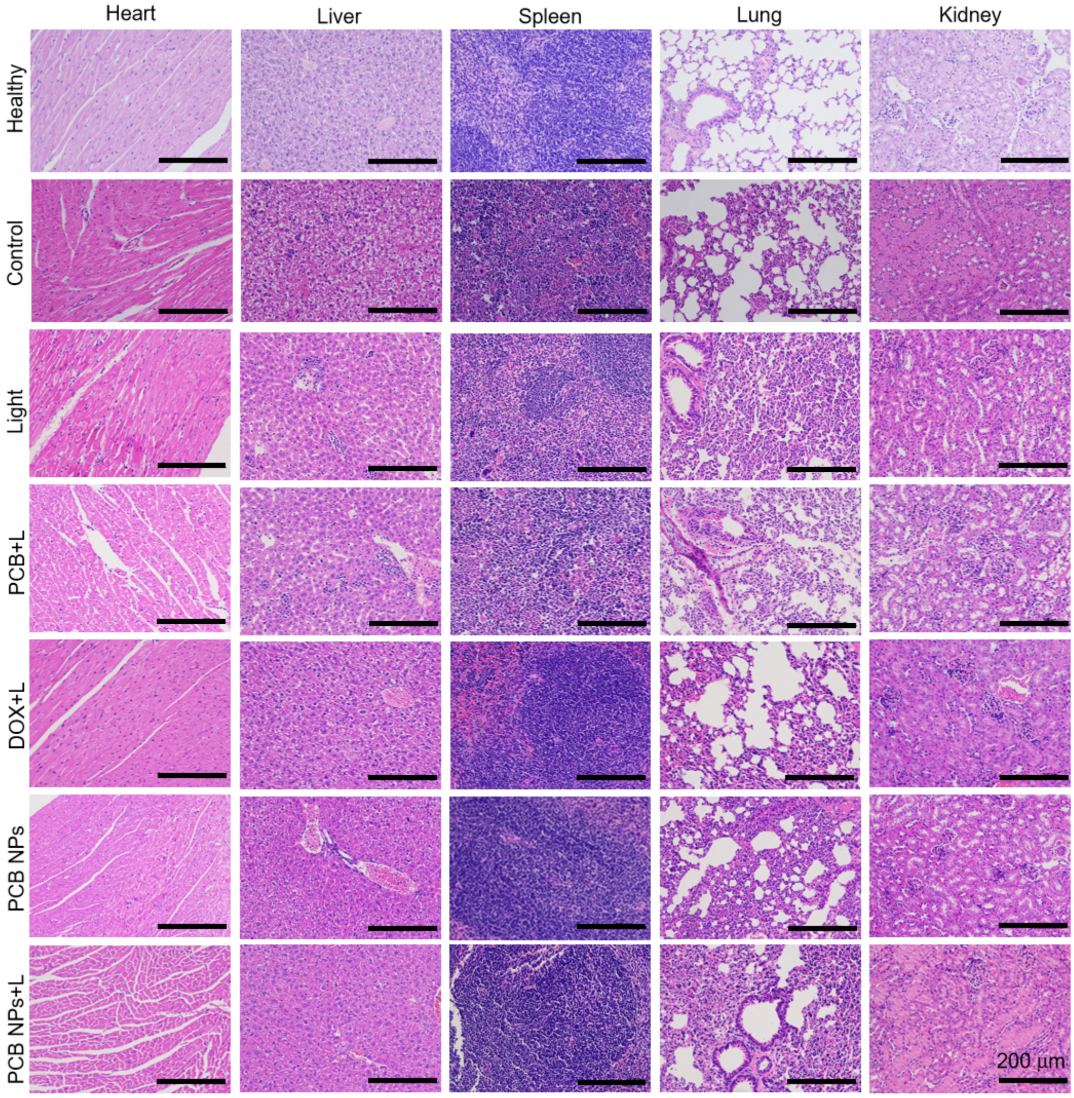

Fig. S24. H&E staining of major organs of the mice after treatment. Scale bar: 200 μm.

Reference

[S1] H. Li, L. Guan, X. Zhang, H. Yu, D. Huang, M. Sun and S. Wang, A cyanine-based near-infrared fluorescent probe for highly sensitive and selective detection of hypochlorous acid and bioimaging, *Talanta*, 2016, **161**, 592-598.